nature materials

ARTICLES

PUBLISHED ONLINE: 6 OCTOBER 2013 | DOI: 10.1038/NMAT3757

Snapshots of non-equilibrium Dirac carrier distributions in graphene

Isabella Gierz[1]★, Jesse C. Petersen[1,2], Matteo Mitrano[1], Cephise Cacho[3], I. C. Edmond Turcu[3], Emma Springate[3], Alexander Stöhr[4], Axel Köhler[4], Ulrich Starke[4] and Andrea Cavalleri[1,2]★

The optical properties of graphene are made unique by the linear band structure and the vanishing density of states at the Dirac point. It has been proposed that even in the absence of a bandgap, a relaxation bottleneck at the Dirac point may allow for population inversion and lasing at arbitrarily long wavelengths. Furthermore, efficient carrier multiplication by impact ionization has been discussed in the context of light harvesting applications. However, all of these effects are difficult to test quantitatively by measuring the transient optical properties alone, as these only indirectly reflect the energy- and momentum-dependent carrier distributions. Here, we use time- and angle-resolved photoemission spectroscopy with femtosecond extreme-ultraviolet pulses to directly probe the non-equilibrium response of Dirac electrons near the K-point of the Brillouin zone. In lightly hole-doped epitaxial graphene samples, we explore excitation in the mid- and near-infrared, both below and above the minimum photon energy for direct interband transitions. Whereas excitation in the mid-infrared results only in heating of the equilibrium carrier distribution, interband excitations give rise to population inversion, suggesting that terahertz lasing may be possible. However, in neither excitation regime do we find any indication of carrier multiplication, questioning the applicability of graphene for light harvesting.

The non-equilibrium dynamics of Dirac electrons in graphene have so far been primarily investigated with time-resolved optical techniques[1–8], yielding precise estimates of the relaxation rates after photo-excitation. However, as optical probing only indirectly measures energy- and momentum-dependent carrier distributions, controversies have arisen over the underlying physics. Crucially, it has not yet been established whether the distribution of hot carriers at early times should be described by a single[2,5,6,8], or by two distinct Fermi–Dirac distributions with different chemical potentials for the valence and conduction bands[1,3,4,9]. Clarification of this issue is essential for assessing the potential of graphene for optoelectronics as it defines whether charge carriers in graphene exhibit a metallic or a semiconducting response to photo-excitation. Furthermore, direct experimental proof of the existence of carrier multiplication[10,11] is lacking. Here, we resolve these questions by directly mapping the transient occupation of electronic states as a function of momentum and energy with photoemission spectroscopy for different time delays after photo-excitation.

The honeycomb lattice of graphene, together with a sketch of the two-dimensional Brillouin zone is shown in Fig. 1a. We studied a quasi-freestanding epitaxial graphene monolayer grown on SiC(0001) (refs 12,13), which was first characterized by static angle-resolved photoemission spectroscopy (ARPES). Figure 1b shows photoelectron energy and momentum maps along and perpendicular to the ΓK-direction, evidencing the well-known conical band structure[14,15] that is responsible for graphene's peculiar optical properties[1,10,11,16–22]. For measurements perpendicular to the ΓK-direction, extrapolation of the bands based on a tight-binding model (dashed lines)[14] shows that the graphene layer is hole-doped, with the Dirac point ~200 meV above the static chemical potential μ_e. For measurements along ΓK, only one of the two π-bands is visible owing to photoemission matrix element effects[23].

The non-equilibrium response of this sample was studied for excitation below and above the minimum photon energy for interband excitations ($2\mu_e = 400$ meV). In this way, both metallic ($\hbar\omega_{\text{pump}} = 300$ meV) and semiconducting ($\hbar\omega_{\text{pump}} = 950$ meV) optical properties were explored. To probe the dynamics of the π-bands at the K-point of the hexagonal Brillouin zone ($k_{\parallel} = 1.7\,\text{Å}^{-1}$, requiring $\hbar\omega_{\text{probe}} > 16$ eV), 30 femtosecond (fs) extreme-ultraviolet (EUV) pulses from a high-harmonic generation source were used[24–26]. A time-preserving monochromator selected a single harmonic at $\hbar\omega_{\text{probe}} = 31.5$ eV with an energy resolution of 130 meV (ref. 27).

Figure 2a shows a schematic of the expected excitation mechanism for photon energies $\hbar\omega_{\text{pump}} < 2|\mu_e|$, for which only free-carrier absorption is possible. For an electromagnetic pulse with vector potential $\mathbf{A}(t) = \int \mathbf{E}\,\mathrm{d}t$, the Dirac electrons are accelerated and decelerated according to the interaction Hamiltonian $\mathbf{H} = (1/2m^*)(\mathbf{p} - q\mathbf{A})^2$, where m^* is the effective mass and $\mathbf{p}$ is the momentum operator. Scattering events with other electrons or with the lattice cause rapid thermalization into a hot carrier distribution.

A set of experimental snapshots of the Dirac cone is plotted in Fig. 2b for different pump–probe delays after excitation at $\hbar\omega_{\text{pump}} = 300$ meV with a fluence of $F = 0.8$ mJ cm^{-2}. Within the time resolution of our measurement we did not resolve non-thermal energy distributions for the Dirac electrons, indicating very efficient thermalization. Rather, we observed instantaneous broadening of the carrier distribution through the Dirac point (Fig. 2b middle panel) and subsequent relaxation within ~1 ps (Fig. 2b right panel).

---

[1]Max Planck Institute for the Structure and Dynamics of Matter, 22761 Hamburg, Germany, [2]Department of Physics, Clarendon Laboratory, University of Oxford, OX1 3PU Oxford, UK, [3]Central Laser Facility, STFC Rutherford Appleton Laboratory, OX11 0QX Harwell, UK, [4]Max Planck Institute for Solid State Research, 70569 Stuttgart, Germany. *e-mail: isabella.gierz@mpsd.cfel.de; andrea.cavalleri@mpsd.cfel.de

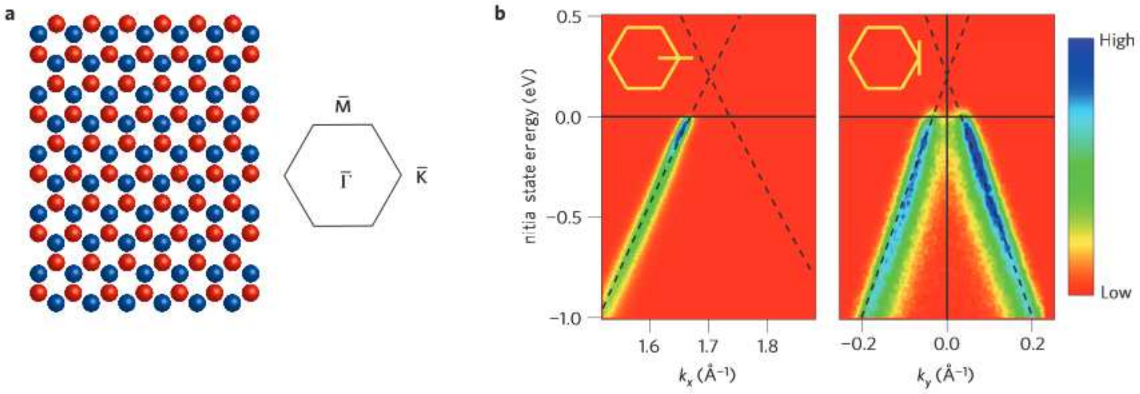

Figure 1 | Atomic and electronic structure of graphene. a, The honeycomb lattice with the hexagonal Brillouin zone. The two triangular sublattices are shown in red and blue, respectively. **b**, Equilibrium band structure measured with linearly polarized synchrotron radiation ($\hbar\omega = 30$ eV, left) and He II radiation ($\hbar\omega = 41$ eV, right). The colour scale is linear with violet (red) corresponding to high (low) photocurrent. The inset shows the cut through the Brillouin zone along which the photoemission data has been measured. Dashed black lines represent the dispersion obtained from a tight-binding model[14].

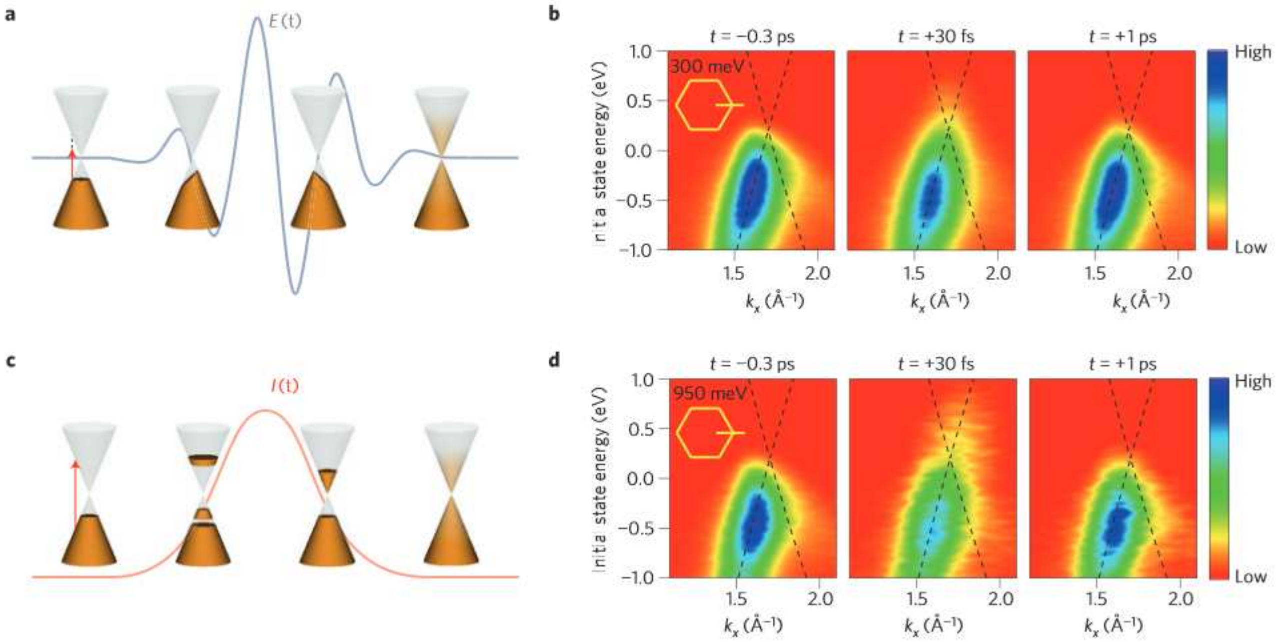

Figure 2 | Free-carrier absorption regime versus direct interband transitions. The panels on the left show schematics of the excitation schemes employed in this work, the panels on the right show corresponding snapshots of the electronic structure measured at $\hbar\omega_{\text{pump}} = 31.5$ eV for different time delays. **a**, Free-carrier absorption for $\hbar\omega_{\text{pump}} < 2\,|\mu_e|$. The light grey line represents the electric field of the pump pulse. **b**, Measured snapshots of the band structure (smoothed) close to the K-point for different pump–probe delays for excitation at $\hbar\omega_{\text{pump}} = 300$ meV $< 2|\mu_e|$ with $F = 0.8$ mJ cm^{-2}. **c**, Direct interband transitions for $\hbar\omega_{\text{pump}} > 2|\mu_e|$. The light red line represents the intensity of the pump pulse. **d**, Measured snapshots for excitation at $\hbar\omega_{\text{pump}} = 950$ meV $> 2\,\mu_e|$ with $F = 4.6$ mJ cm^{-2}. The measurements (**b**,**d**) were done along the ΓK-direction (insets). Dashed black lines represent the dispersion obtained from a tight-binding model[14].

A quantitative analysis of these dynamics is shown in Fig. 3. In Fig. 3a we show energy distribution curves (EDCs) that have been integrated at each time delay over the momentum range depicted in Fig. 2b. Zero delay corresponds to the maximum pump–probe signal. The energy dependence of the EDCs is well fitted at all times by the Fermi–Dirac distribution $f(E, \mu_e, T_e) = (\exp((E - \mu_e/k_B T_e)) + 1)^{-1}$, where E is the energy, k_B is the Boltzmann constant, and T_e is the electronic temperature. The broadening of the Fermi edge immediately after absorption of the pump pulse reflects an increase in T_e that subsequently cools down to room temperature within ~1 ps. Figure 3b shows EDCs for selected time delays (~0.3 ps (blue), 0 ps (red) and +0.5 ps (green)) together with Fermi–Dirac fits (black lines). Fit results for μ_e and T_e are shown in Fig. 3c,d, respectively.

The chemical potential initially increases by approximately 40 meV, recovering as the carriers cool. The initial increase and fast decay of the chemical potential is well understood as a consequence of the changes in electronic temperature (Fig. 3d), as $\Delta\mu = (\pi^2/6)(k_B T_e)^2/E_F$ (ref. 28), where E_F is the Fermi energy.

The time-dependent electronic temperature $T_e(t)$ is shown in Fig. 3d. T_e is observed to instantly rise to nearly 3,000 K, before decaying with a triple exponential law (black line in Fig. 3d), in excellent agreement with previous all-optical measurements. These measurements have attributed the decay channels to electron–

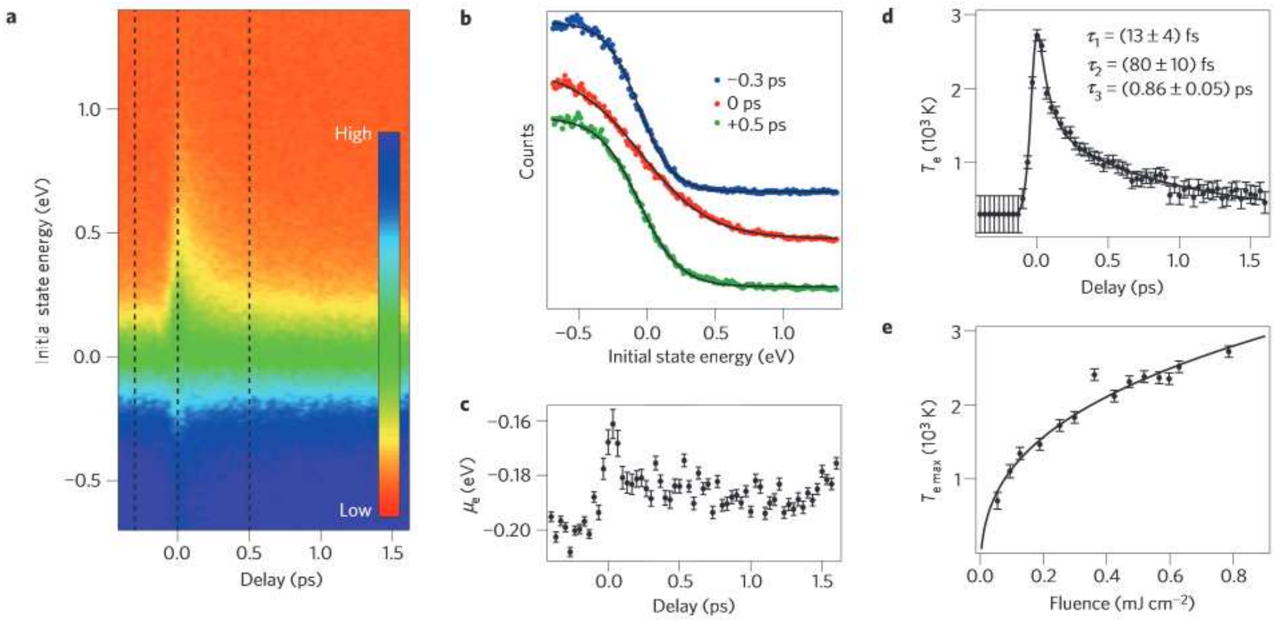

Figure 3 | Metallic response for excitation at $\hbar\omega_{\text{pump}} = 300$ meV and $F = 0.8$ mJ cm^{-2}. a, EDCs integrated over the momentum range shown in Fig. 2b as a function of delay in a two-dimensional colour plot. **b**, Selected EDCs extracted along the dashed lines in **a** together with Fermi–Dirac distribution fits that are shown as solid black lines. **c**,**d**, Chemical potential (**c**) and electronic temperature (**d**) as a function of delay. The solid black line in **d** is a fit including an error function for the rise time and three exponential decays: $\tau_1 = (13 \pm 4)$ fs, $\tau_2 = (80 \pm 10)$ fs and $\tau_3 = (0.86 \pm 0.05)$ ps, consistent with the results of all-optical measurements. **e**, The fluence dependence of the maximum electronic temperature follows the $F^{1/3}$ behaviour (black line) expected for free-carrier absorption. Error bars represent the standard deviation of the fitting parameters.

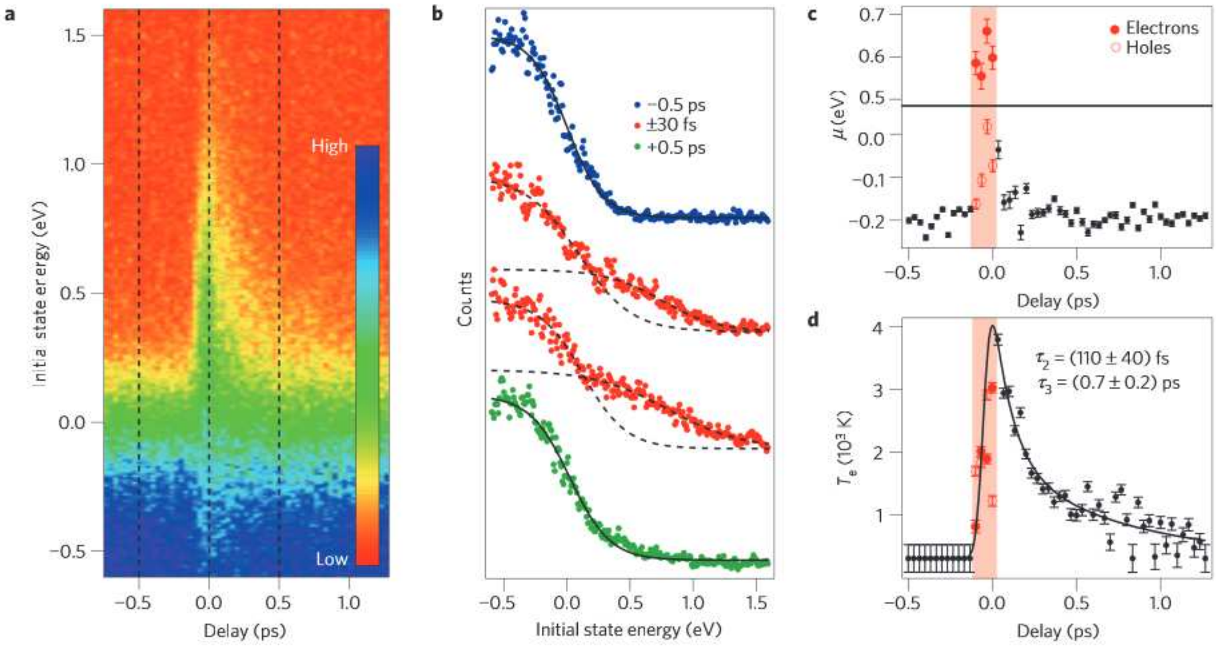

Figure 4 | Population inversion for excitation at $\hbar\omega_{\text{pump}} = 950$ meV and $F = 4.6$ mJ cm^{-2}. a, Momentum-integrated EDCs as a function of delay. **b**, EDCs for three selected delays extracted along the dashed lines in **a** together with Fermi–Dirac distribution fits. The EDCs close to time zero are best fitted with two distinct Fermi–Dirac distributions for electrons and holes (dashed black lines). **c**,**d**, Chemical potential (**c**) and electronic temperature (**d**) as a function of delay. The red-shaded area indicates the time interval over which two distinct Fermi–Dirac distributions persist. The solid black line in **d** represents a fit of the black data points with a fixed rise time of 50 fs and a double exponential decay. The decay times are indicated in the figure. Error bars represent the standard deviation of the fitting parameters.

electron scattering (τ_1; refs 3,4), emission of optical phonons (τ_2; refs 5–7,29), and further cooling through the decay of optical into acoustic phonons (τ_3 ; refs 8,30–33). More recently, the third relaxation time τ_3 has been ascribed to the direct coupling between electrons and acoustic phonons in the presence of lattice defects[34,35]. Our data are consistent with both interpretations of τ_3. A validation of the decay law would require temperature-dependent measurements that are beyond the scope of his paper.

The fluence dependence of the peak electronic temperature, which further substantiates the physical picture discussed above,

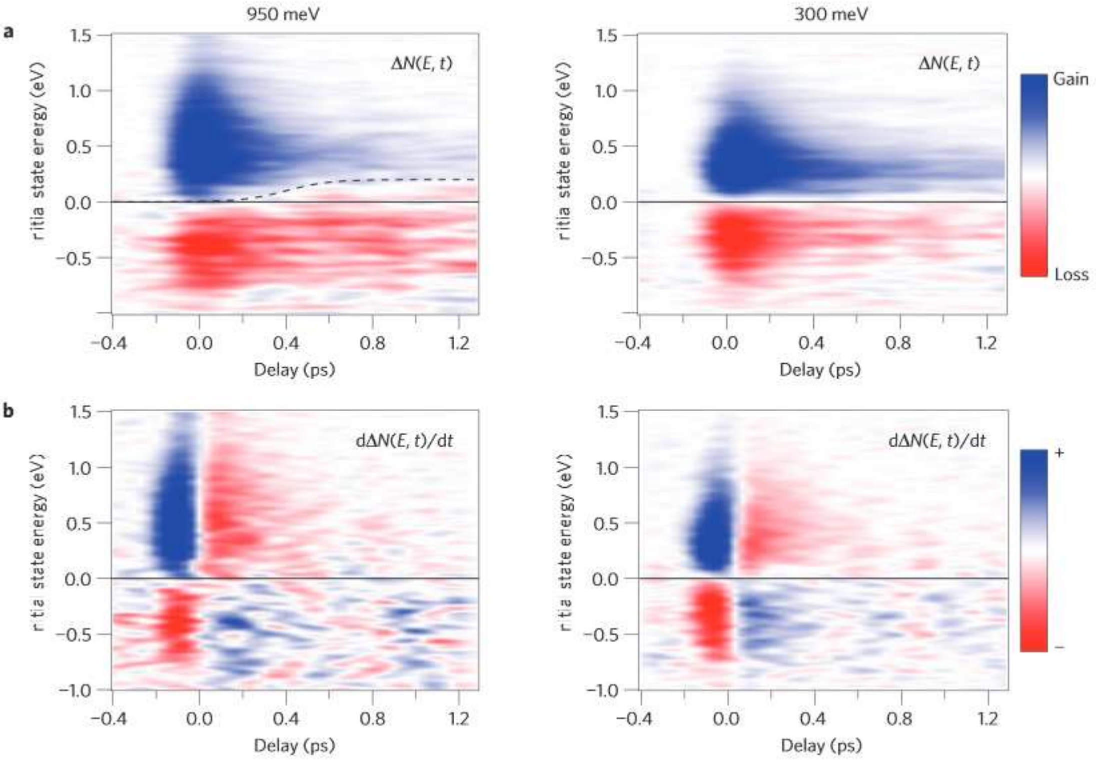

Figure 5 | No indication for carrier multiplication. a,b, Change in occupancy $\Delta N(E,t)$ (**a**) and its time derivative $\mathrm{d}\Delta N(E,t)/\mathrm{d}t$ (**b**) as a function of energy and delay. No carrier multiplication is found for direct interband transitions (left column) or free-carrier absorption (right column). $\Delta N(E,t)$ is obtained as the difference between the photocurrent shown in Figs 3a and 4a, respectively, and the photocurrent at negative time delays. The dashed line in **a** is a guide to the eye that emphasizes the energy at which $\Delta N(E,t)=0$, that is, where the pump probe signal changes sign.

is shown in Fig. 3e. The increase in kinetic energy of the Dirac carriers can be obtained from $\Delta E=\int_{\mu_e}^{\infty}\mathrm{DOS}(E)f(E,\mu_e,T_e)E\,\mathrm{d}E$, where $\mathrm{DOS}(E)\propto|E|$ is the linear density of states of graphene. For simplicity, we choose $\mu_e(T_e)=0$ and obtain $\Delta E\propto T_e^3$, where ΔE is equivalent to the absorbed F in mJ cm^{-2}. The experimental fluence dependence of T_e, shown in Fig. 3e, follows the expected $F^{1/3}$ behaviour (black line).

We next report results for direct interband excitation at $\hbar\omega_{\mathrm{pump}}=950$ meV in Figs 2c,d and 4. Figure 2c shows a schematic of the expected interband excitation mechanism, which, in contrast to the free-carrier absorption discussed above, is driven by the intensity envelope $I(t)$ of the laser pulse (red line) rather than the electric field. During interband excitation, a non-thermal distribution of excited electron–hole pairs is generated at the earliest time delays, relaxing into a quasi-equilibrium state with a temperature higher than that of the lattice. Importantly, depending on the relative strength of interband versus intraband scattering, a single metallic distribution such as the one of Fig. 3b, or two distinct distributions for the valence and conduction bands are attained. Only the latter scenario would make light amplification possible[1,19,20].

In Fig. 2d we present snapshots of the Dirac carrier distributions for different time delays after excitation at $\hbar\omega_{\mathrm{pump}}=950$ meV and $F=4.6$ mJ cm^{-2}. The excitation fluence was chosen according to experimental estimates of the threshold for optical gain in ref. 1.

Figure 4a,b reports momentum-integrated EDCs as a function of pump–probe delay. In contrast to Fig. 3b, the carrier distributions measured immediately after excitation are best fitted by two separate Fermi–Dirac distributions for the valence and conduction bands, indicating population inversion[1]. The fit results for μ_e and the T_e are shown in Fig. 4c,d, respectively. The two distributions merge within ~130 fs, and a single Fermi–Dirac distribution is attained, promoted by scattering of charge carriers across the Dirac point. As amplification is possible only for the given time window[1,9], our measurement sets a quantitative boundary to be used as a benchmark for any laser design.

Our measurements also provide a direct assessment of the possibility of carrier multiplication in graphene[10,11]. Figure 5 shows the time-dependent evolution of the pump–probe signal for the two cases of free-carrier absorption (right panel) and interband excitation (left panel). Specifically, Fig. 5a shows the pump-induced changes of the photocurrent (directly proportional to the number of electrons N at energy E) as a function of energy and time delay. Blue (red) corresponds to a gain (loss) in photocurrent with respect to negative time delays. Note that for energies just above the Fermi level, the energy E for which the pump–probe signal is zero, drifts upward in energy over a timescale of 0.4 ps (dashed black line in the left panel of Fig. 5a). Similar sign changes in optical pump–probe signals have been attributed to bandgap renormalization[3,4]. In Fig. 5b, the time derivative of the pump–probe signal of Fig. 5a is shown, directly revealing the electron–hole pair generation/recombination rates. The generation/recombination rate $\mathrm{d}\Delta N(E>0,t)/\mathrm{d}t$ is positive only for a few tens of femtoseconds. We conclude that electron–hole pairs are generated only while the pump pulse is present, whereas no spontaneous carrier multiplication is found.

The reason why carrier multiplication does not occur can be inferred by comparing the phase space available for impact ionization (where the excess energy of a photo-excited electron is used to generate another electron–hole pair) and Auger heating (where the energy that is released during recombination of an electron–hole pair is absorbed by another electron in the conduction band), respectively, as sketched in Fig. 6. Carrier multiplication after photo-excitation can occur only if impact ionization dominates over other competing relaxation channels such as Auger heating or emission of phonons. References 10,11

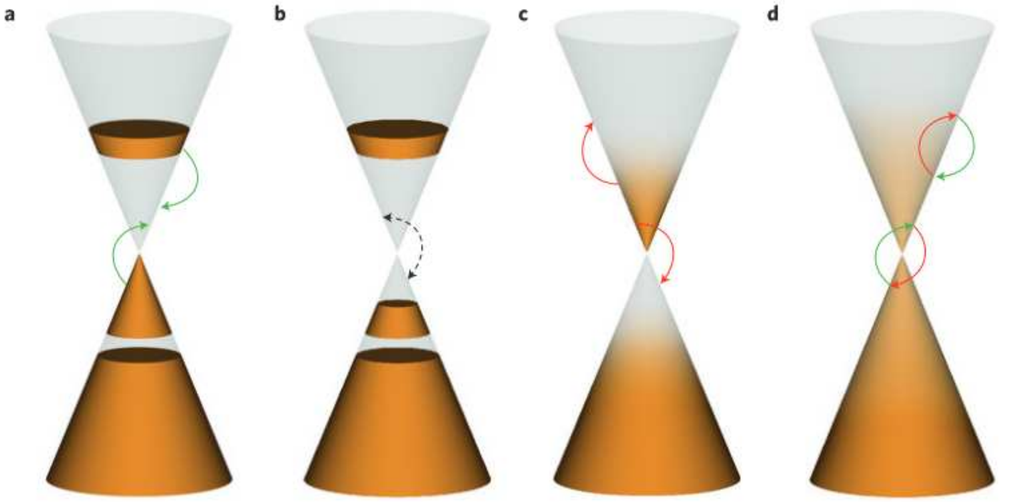

Figure 6 | Competition between impact ionization and Auger heating in graphene. a, The initial non-thermal electron distribution attained immediately after absorption of the pump pulse offers a large phase space for impact ionization (green arrows) while inhibiting the inverse process of Auger heating, theoretically enabling carrier multiplication in an undoped sample[10,11]. **b**, For a hole-doped sample the absence of electrons close to the Dirac point inhibits both impact ionization and Auger heating. The resulting suppression of interband scattering (dashed black arrow) leads to the formation of population inversion. **c**, For a population-inverted state the onset of Auger heating (red arrows) rapidly merges the separate chemical potentials. **d**, Once a single hot electronic distribution is established, impact ionization and Auger heating are equally likely with zero net effect, and the electronic system can cool down only through phonon emission.

predicted that the highly non-thermal electronic distribution immediately after photo-excitation for an undoped graphene sample results in efficient impact ionization, simultaneous suppression of Auger heating and, hence, carrier multiplication (Fig. 6a). For a hole-doped graphene layer with the Dirac point above the Fermi level, neither impact ionization nor Auger heating can occur near the Dirac point (Fig. 6b). The resulting absence of interband scattering results in population inversion as observed in Fig. 4. In the presence of two distinct Fermi–Dirac distributions (Fig. 6c) impact ionization can create additional electron–hole pairs only if the temperature of the Dirac carriers k_BT_e exceeds the sum of the electron and hole chemical potentials $|\mu_e| + |\mu_h|$. This would require temperatures above ~8,000 K, significantly higher than the peak temperature of ~4,000 K estimated in Fig. 4. Instead, the inverse scattering process (Auger heating) dominates, rapidly merging the separate chemical potentials. For a single Fermi–Dirac distribution (Fig. 6d) attained ~130 fs after direct interband transitions or at all times for free-carrier absorption, the probabilities for impact ionization and Auger heating are similar, again preventing carrier multiplication.

The absence of carrier multiplication and the short lifetime of electron–hole pairs discussed above raises serious doubts about the suitability of graphene for efficient light harvesting, at least in the present excitation regime. One may speculate that more favourable conditions for carrier multiplication may be met for negligible doping of the graphene layer, smaller pump fluences and higher excitation energies[11].

In summary, we have used time- and angle-resolved photoemission in the EUV as a tool to critically assess the potential of graphene for optoelectronic applications. Two key contributions are presented. First, we show that population inversion occurs immediately after interband excitation, substantiating the view of graphene as a zero-bandgap semiconductor. Previous time-resolved optical experiments had evidenced negative optical conductivity (optical gain)[1]. However, these measurements probed only at higher photon energies and could not detect the dynamics close to the Dirac point. The present experiment allows for a direct measurement down to arbitrarily small energies and with a temporal resolution that would not be possible for terahertz optical probes. Second, by directly measuring the band occupancy $N(E,t)$ at all energies and times, we have made a quantitative evaluation of the relevance of carrier multiplication.

Direct mapping of the non-equilibrium carrier distribution and primary acceleration/scattering events with a few femtosecond or even attosecond resolution[36] is clearly a highly interesting area of future research. Combining ultrafast photoemission techniques with nanoscale spatial resolution, for example in photoemission electron microscopy, would make it possible to investigate nanoscale carrier dynamics as well as real device transport.

Note added in proof: related work has recently been published in ref. 37.

Methods

Details about the sample growth are reported in refs 12,13. The SiC(0001) substrate was etched in a hydrogen atmosphere to produce atomically flat terraces. In a second step, the substrate was annealed in inert argon gas to grow a homogeneous carbon monolayer that was subsequently decoupled from the substrate by hydrogen intercalation, resulting in a completely sp^2-hybridized graphene layer. After growth, the samples were transported in air and inserted into an ultrahigh vacuum chamber, where the samples were annealed at about 500 °C to remove adsorbates, and characterized with static ARPES. Measurements at the K-point perpendicular to the ΓK-direction were performed at the Max Planck Institute for Solid State Research in Stuttgart (Germany) with helium II radiation at $\hbar\omega = 41$ eV. The static ARPES measurement along the ΓK-direction was carried out at the Swiss Light Source (SLS) of the Paul Scherrer Institute (Villigen) with a photon energy of $\hbar\omega = 30$ eV and linearly polarized light. Measurements at the SLS were performed on a different sample[13] (but grown following the same recipe) from the other static and time-resolved experiments in the manuscript.

Time-resolved ARPES measurements were performed at the Materials Science end-station at Artemis (Central Laser Facility), using synchronized near-infrared and EUV photons as pump and probe pulses, respectively. The facility is equipped with a 1 kHz Ti:sapphire laser system that delivers pulses with a central wavelength of 790 nm and a nominal pulse duration of 30 fs. Near-infrared photons are generated through optical parametric amplification (950 meV) and subsequent difference frequency generation (300 meV). EUV photons in the range from 20 to 40 eV are obtained through high-harmonic generation in an argon gas jet. For the present experiment a photon energy of $\hbar\omega_{\text{probe}} = 31.5$ eV was chosen, using a time-preserving monochromator to maintain a short pulse, enabling access to electrons emitted at the K-point of the two-dimensional graphene Brillouin zone.

All measurements in this paper were performed at room temperature, except the static dispersion along the ΓK-direction shown in Fig. 1b, which was acquired at a sample temperature of 70 K.

The EDCs in Figs 3 and 4 were fitted with a Fermi–Dirac function convoluted with a Gaussian to account for the finite experimental resolution. The width of the Gaussian was fixed to 130 meV, which resulted in an electronic temperature of 300 K for the energy distribution curves at negative time delays.

Received 16 April 2013; accepted 20 July 2013; published online 6 October 2013

References

1. Li, T. *et al.* Femtosecond population inversion and stimulated emission of dense Dirac fermions in graphene. *Phys. Rev. Lett.* **108,** 167401 (2012).
2. Sun, D. *et al.* Ultrafast relaxation of excited Dirac fermions in epitaxial graphene using optical differential transmission spectroscopy. *Phys. Rev. Lett.* **101,** 157402 (2008).
3. Breusing, M., Ropers, C. & Elsaesser, T. Ultrafast carrier dynamics in graphite. *Phys. Rev. Lett.* **102,** 086809 (2009).
4. Breusing, M. *et al.* Ultrafast nonequilibrium carrier dynamics in a single graphene layer. *Phys. Rev. B* **83,** 153410 (2011).
5. Kampfrath, T., Perfetti, L., Schapper, F., Frischkorn, C. & Wolf, M. Strongly coupled optical phonons in the ultrafast dynamics of the electronic energy and current relaxation in graphite. *Phys. Rev. Lett.* **95,** 187403 (2005).
6. Lui, C. H., Mak, K. F., Shan, J. & Heinz, T. F. Ultrafast photoluminescence from graphene. *Phys. Rev. Lett.* **105,** 127404 (2010).
7. George, P. A. *et al.* Ultrafast optical-pump terahertz-probe spectroscopy of the carrier relaxation and recombination dynamics in epitaxial graphene. *Nano Lett.* **8,** 4248–4251 (2008).
8. Wang, H. *et al.* Ultrafast relaxation dynamics of hot optical phonons in graphene. *Appl. Phys. Lett.* **96,** 081917 (2010).
9. Gilbertson, S. *et al.* Tracing ultrafast separation and coalescence of carrier distributions in graphene with time-resolved photoemission. *J. Phys. Chem. Lett.* **3,** 64–68 (2012).
10. Winzer, T., Knorr, A. & Malić, E. Carrier multiplication in graphene. *Nano Lett.* **10,** 4839–4843 (2010).
11. Winzer, T. & Malić, E. Impact of Auger processes on carrier dynamics in graphene. *Phys. Rev. B* **85,** 241404(R) (2012).
12. Riedl, C., Coletti, C., Iwasaki, T., Zakharov, A. A. & Starke, U. Quasi-free-standing epitaxial graphene on SiC obtained by hydrogen intercalation. *Phys. Rev. Lett.* **103,** 246804 (2009).
13. Forti, S. *et al.* Large-area homogeneous quasifree standing epitaxial graphene on SiC(0001): Electronic and structural characterization. *Phys. Rev. B* **84,** 125449 (2011).
14. Bostwick, A., Ohta, T., Seyller, T., Horn, K. & Rotenberg, E. Quasiparticle dynamics in graphene. *Nature Phys.* **3,** 36–40 (2007).
15. Bostwick, A. *et al.* Observation of plasmarons in quasi-freestanding doped graphene. *Science* **328,** 999–1002 (2010).
16. Nair, R. R. *et al.* Fine structure constant defines visual transparency of graphene. *Science* **320,** 1308 (2008).
17. Bao, Q. *et al.* Atomic-layer graphene as a saturable absorber for ultrafast pulsed lasers. *Adv. Funct. Mater.* **19,** 3077–3083 (2009).
18. Sun, Z. *et al.* Graphene mode-locked ultrafast laser. *ACS Nano* **4,** 803–810 (2010).
19. Ryzhii, V., Ryzhii, M. & Otsuji, T. Negative dynamic conductivity of graphene with optical pumping. *J. Appl. Phys.* **101,** 083114 (2007).
20. Winzer, T., Malić, E. & Knorr, A. Microscopic mechanism for transient population inversion and optical gain in graphene. Preprint at http://arxiv.org/abs/1209.4833v1 (2012).
21. Bonaccorso, F., Sun, Z., Hasan, T. & Ferrari, A. C. Graphene photonics and optoelectronics. *Nature Photon.* **4,** 611–622 (2010).
22. Gabor, N. M. *et al.* Hot carrier-assisted intrinsic photoresponse in graphene. *Science* **334,** 648–652 (2011).
23. Shirley, E. L., Terminello, L. J., Santoni, A. & Himpsel, F. J. Brillouin-zone-selection effects in graphite photoelectron angular distributions. *Phys. Rev. B* **51,** 13614 (1995).
24. Mathias, S. *et al.* Angle-resolved photoemission spectroscopy with a femtosecond high harmonic light source using a two-dimensional imaging electron analyzer. *Rev. Sci. Instrum.* **78,** 083105 (2007).
25. Rohwer, T. *et al.* Collapse of long-range charge order tracked by time-resolved photoemission at high momenta. *Nature* **471,** 490–493 (2011).
26. Petersen, J. C. *et al.* Clocking the melting transition of charge and lattice order in 1T-TaS$_2$ with ultrafast extreme- ultraviolet angle-resolved photoemission spectroscopy. *Phys. Rev. Lett.* **107,** 177402 (2011).
27. Frassetto, F. *et al.* Single-grating monochromator for extreme-ultraviolet ultrashort pulses. *Opt. Express* **19,** 19169–19181 (2011).
28. Ashcroft, N. W. & Mermin, N. D. *Solid State Physics* (Thomson Learning, 1976).
29. Butscher, S., Milde, F., Hirtschulz, M., Malić, E. & Knorr, A. Hot electron relaxation and phonon dynamics in graphene. *Appl. Phys. Lett.* **91,** 203103 (2007).
30. Bonini, N., Lazzeri, M., Marzari, N. & Mauri, F. Phonon anharmonicities in graphite and graphene. *Phys. Rev. Lett.* **99,** 176802 (2007).
31. Yan, H. *et al.* Time-resolved Raman spectroscopy of optical phonons in graphite: Phonon anharmonic coupling and anomalous stiffening. *Phys. Rev. B* **80,** 121403(R) (2009).
32. Kang, K., Abdula, D., Cahill, D. G. & Shim, M. Lifetimes of optical phonons in graphene and graphite by time-resolved incoherent anti-Stokes Raman scattering. *Phys. Rev. B* **81,** 165405 (2010).
33. Sun, D. *et al.* Ultrafast relaxation of excited Dirac fermions in epitaxial graphene using optical differential transmission spectroscopy. *Phys. Rev. Lett.* **104,** 136802 (2010).
34. Song, J. C. W., Reizer, M. Y. & Levitov, L. S. Disorder-assisted electron-phonon scattering and cooling pathways in graphene. *Phys. Rev. Lett.* **109,** 106602 (2012).
35. Graham, M. W., Shi, S-F., Ralph, D. C., Park, J. & McEuen, P, L. Photocurrent measurements of supercollision cooling in graphene. *Nature Phys.* **9,** 103–108 (2013).
36. Cavalieri, A. L. *et al.* Attosecond spectroscopy in condensed matter. *Nature* **449,** 1029–1032 (2007).
37. Johannsen, J. C. *et al.* Direct view of hot carrier dynamics in graphene. *Phys. Rev. Lett.* **111,** 027403 (2013).

Acknowledgements

We thank M. Eckstein and F. Kärtner for many fruitful discussions and J. Harms for drawing Figs 2a,c and 6. S. Forti, C. Coletti and K. V. Emtsev helped with the static ARPES measurements at the SLS, partially supported by the German Research Foundation (DFG) within the priority programme 'graphene' SPP 1459 (Sta 315/8-1). P. Rice, R. Chapman and N. Rodrigues are acknowledged for technical support during the Artemis beam time that was funded by LASERLAB-EUROPE (EC FP7).

Author contributions

I.G., J.C.P., M.M. and C.C. performed the time-resolved experiments. E.S. managed the laboratory and I.C.E.T. ran the laser system; both I.C.E.T. and E.S. provided technical support during the beam time. A.S., A.K. and U.S. grew and characterized the samples. I.G. analysed the data. I.G. and A.C. interpreted the results and wrote the manuscript.

Additional information

Reprints and permissions information is available online at www.nature.com/reprints. Correspondence and requests for materials should be addressed to I.G. or A.C.

Competing financial interests

The authors declare no competing financial interests.